width of the spectral response function (Parry, 1984), and therefore does not predict any effect.

To test this, we recorded speckle data as a function of the incident x-ray energy across the Zn L_3 edge (1021 eV) in metallic zinc powder samples consisting of ~100 nm grains supported on 200-nm-thick silicon nitride membranes. The disordered powder samples were illuminated with a nearly (92%) coherent, 10-µm-diameter x-ray beam. We found by analyzing the intensity auto-correlation function of the data that the speckle contrast decreases as the absorption cross section increases at the edge (Fig. 1.25), indicating that standard speckle theory is indeed invalid near absorption edges (Retsch & McNulty, 2001). Speckle data taken across the K edge of a powdered aluminum sample (1560 eV) yielded comparable results. This effect has already been exploited to enhance speckle originating from a constituent element in a sample, e.g., to study ordering in anti-ferromagnetic domains. In addition to these applications, edge-dependent contrast variations should be well understood if pre-, on-, and post-edge measurements are to be compared in coherent scattering experiments.

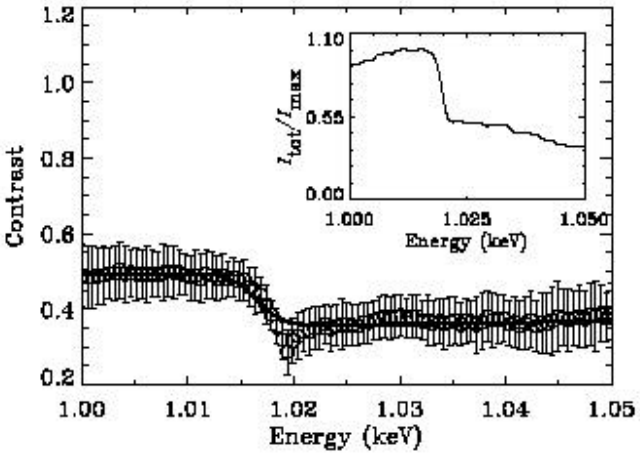

Fig. 1.25. X-ray speckle contrast versus energy in Zn powder (1.8-eV resolution), averaged over a small region of reciprocal space. The solid line shows a theoretical fit to the data points. Inset shows the total transmitted intensity measured directly behind the sample, normalized by the beamline efficiency.

1.8 New Techniques and Instrumentation

Several technical enhancements supported our activities. We acquired a state-of-the-art visible fluorescence microscope and developed a precision kinematic sample holder that enables correlative visible and x-ray microscope studies as well as fast positioning of specimens with 1 µm accuracy. The 2-ID-E fluorescence microprobe was upgraded with a motorized table and curved rails allowing rapid and repeatable energy changes. We developed a compact, modular soft x-ray "nanoprobe" that permits rapid and reproducible optics alignment in the soft x-ray scanning microscope and diffractometer. Other key instrumentation developments included a quantitative x-ray beam coherence diagnostic, commissioning of the 2-BM broad-band double-multilayer monochromator, a major upgrade of the fast microtomography system, integration of the hard x-ray microprobe with a six-circle diffractometer, and fabrication of high-aspect-ratio "lobster-eye" and antiscatter collimators by deep x-ray lithography.

1.8.1 Spatial Coherence Measurement

The dream of creating intense, highly coherent x-ray beams is fueled by the tantalization of new coherence-based x-ray experiments, as well as by existing techniques, such as scanning microscopy, interferometry, coherent scattering, and phase measurement. Thus there is strong motivation

to develop an efficient means to measure the spatial coherence of x-ray beams. We performed a Young's two-slit interference experiment in the soft x-ray region at the 2-ID-B beamline and used it to measure the dependence of the spatial coherence of the x-ray beam on the exit slit of the beamline monochromator. Narrowing the exit slit increases the degree of spatial coherence $|\mu_{12}|$ of the beam, which is directly related to the visibility of the interference fringes produced in a Young's experiment. The Young's slits were fabricated an array of seven slit pairs with 10–200 μm separation in gold. The interference patterns were measured with a scanning avalanche photodiode detector masked with a 5 μm slit. The fringe visibility decreased as the exit slit was widened and as the Young's slit separation was increased (Fig. 1.26), in keeping with expectation. The data showed the beam to have high coherence at Young's slit separations up to 100 μm, in good agreement with the predicted coherence profile (Paterson et al., 2001). A complete measurement of the coherence function requires determination of the degree of coherence over the full range of slit separations in the beam (a time-consuming experiment by the Young's method). Developing a faster approach is the focus of continuing research.

1.8.2 The 2-BM Double-Multilayer Monochromator

We significantly enhanced the capabilities of the 2-BM beamline by incorporating a double-multilayer monochromator (DMM) into it (Chu et al., 2002). The first to be installed at the APS, the DMM was designed and constructed entirely in-house. Because multilayer optics typically have bandwidths ~100 times larger than crystal optics, methods that do not require a high degree of monochromaticity, such as x-ray tomography and fluorescence, benefit tremendously from the greater flux using a DMM. Figure 1.27 shows the DMM design and summarizes its two operating modes. In the normal mode, the DMM optics are inserted into the pink beam reflected by the M1 mirror at 2-BM. Four multilayer coatings allow continuous operation from 3.2-10.9 keV over a 1.35-1.90° incident angular range using the first-order reflection (Table 1.1). The coatings were deposited by DC magnetron sputtering on two 100 mm by 146 mm single-crystal

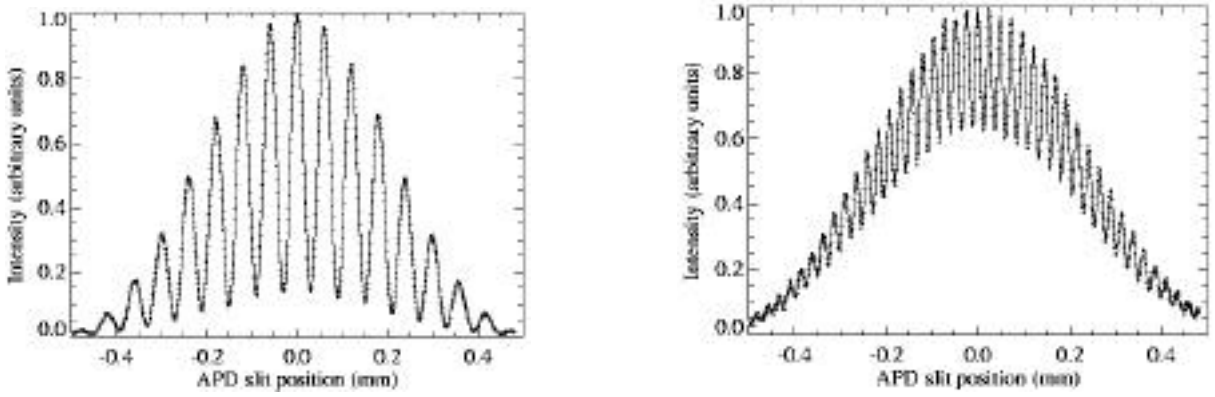

Fig. 1.26. Young's two-slit interference pattern recorded with 1.1 keV x-rays. The solid line is a theoretical fit to the data points. Young's slit separation of (a) 20 μm and (b) 50 μm.

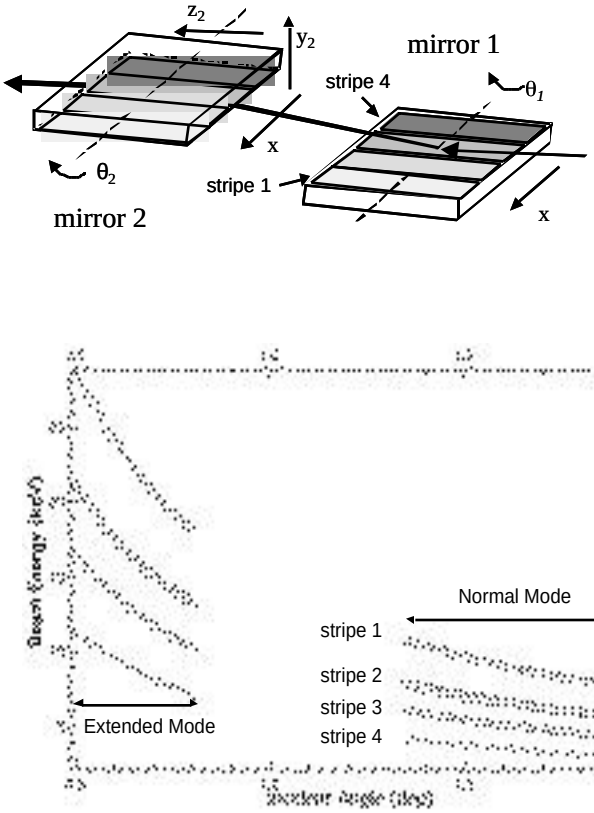

Fig. 1.27. (a) Schematic view of the DMM. Arrows indicate the allowed independent θ_1, θ_2, y_2, z_2 and coupled x motions. (b) The normal operating mode continuously covers 3.2 to 10.9 keV. The extended mode allows operation up to 28 keV using only stripe 2.

.

silicon substrates polished to 1 Å rms roughness and 0.4 µrad average slope error. All four coatings exhibit excellent reflectivity and minimal interfacial roughness and diffuseness (2-3 Å). In the normal operating mode, the DMM provides a fixed exit beam at the same position in the end-station as that from the 2-BM double-crystal monochromator (DCM). However, the DMM delivers 20-40 times more flux than the Si(111) DCM due to its greater bandpass. The DMM also operates in an extended mode at incidence angles of ~0.5-0.8°, giving access to a much wider energy range than originally intended. While the measured bandwidth is 3-4%, the practical flux gain at energies above 13.5 keV in this mode is much greater because the DCM can only reach these energies using the Si(333) reflection, which passes about 10 times lower flux than a Si(111) reflection.

1.8.3 Microtomography System Upgrade

During the last year, the 2-BM fast x-ray microtomography system underwent major upgrades, both in the instrumentation and in the parallel computer cluster used for data analysis (DeCarlo et al., 2002). The data

Table 1.1. Performance of the DMM optics.

Stripe	Multilayer structure	Measured reflectivity at 10 keV	Normal operating energy range	Reflectivity at operating energy range	Bandwidth at operating energy range
1	$[W(7.5) / Si(55.0)]_{35}$	78%	3.2-4.6 keV	~45%	~5%
2	$[W(9.7) / C(14.8)]_{100}$	65%	8.0-10.9 keV	~65%	~1.5%
3	$[W(14.2) / C(19.5)]_{50}$	82%	6.1-8.1 keV	~75%	~5.5%
4	$[W(6.8) / Si(36.0)]_{60}$	83%	4.6-6.4 keV	~65%	~4%

acquisition and analysis systems were completely automated. Both the sample and CCD camera staging were redesigned. We now have a more precise and compact system that allows users to mount and align samples in a few minutes. A newly designed robot allows automatic sample loader capability. The computer cluster was upgraded with 32 CPUs on a dedicated optical fiber 1 Gbit/s subnet. The total reconstruction time is 90 s for a 3D volume of 512^3 pixels and 420 s for a 1024^3 pixel volume. We are also investigating new cluster topologies to further improve these results. Combined with the dedicated reconstruction computer cluster and the higher flux delivered by the 2-BM DMM, these system innovations provide the scientific community with a fast, reliable, remotely controllable, easy-to-use 3D x-ray imaging tool with ~1 μm spatial resolution and ~1 mm field of view.

1.8.4 Integration of a Hard X-ray Microprobe and Six-Circle Diffractometer

X-ray microdiffraction combines conventional diffraction techniques with x-ray microbeam capabilities to achieve spatially resolved phase, crystallographic, and strain information about materials. We have completed the design and construction of a Fresnel-zone-plate-based hard x-ray microprobe (HXRM), and integrated it into a six-circle "kappa" diffractometer for microdiffraction studies at the 2-ID-D beamline (Libera et al., 2002). The kappa geometry accommodates the HXRM in the tight region near the specimen, providing wider access to reciprocal space. The HXRM employs gold phase zone plates with focal lengths of 10 cm and 40 cm (at 8 keV) for high and moderate focusing power. The 10 cm and 40 cm zone plates have diameters of 150 μm and 250 μm, outmost zone widths of 0.1 μm and 0.25 μm, and focal efficiency of 18% and 25% for 8 keV x-rays, respectively. We measured photon fluxes of 1.0×10^{10} and 1.1×10^{11} ph/s/0.01% BW at their foci, corresponding to photon density gains of 15000 and 8000. A two-zone-plate stack was implemented in the HXRM to further improve focusing efficiency, especially at higher energies; gains as high as 3.5 were measured with 10 cm zone plates at 10 keV. Precise alignment of the two zone plates is determined by monitoring the resultant interference pattern (Fig. 1.28, left). The stability of the focal spot and sample position characterizes the performance of the instrument. The HXRM table is supported directly by the diffractometer at one end; a structural steel weldment reinforced with steel webs supports the other end on the same granite base (Fig. 1.28, right). The measured effective beam size is less than 250 nm (Xu et al., 2002).

1.8.5 Fabrication of X-ray Optics by Deep X-ray Lithography

Our deep x-ray lithography (DXRL) program has concentrated on producing 1-mm- to 1- cm- thick structures for advanced accelerator and x-ray instrumentation applications. The facilities, masks, preparation, and processing for 1-mm-thick PMMA photoresists developed so far allow us to fabricate various x-ray optical elements, such as refractive lenses, lobster-eye lenses, and x-ray collimating grids. Lobster-eye optics, square-packed arrays of square channels so-called for their similarity to the eyes of the macruran crustaceans, show great promise as the focusing optic in the next generation of x-ray all-sky monitors. We produced high-aspect-ratio lobster-eye optics using the LIGA process with a graphite substrate (Peele et al., 2001). In the medical field, conventional diagnostic mammography systems for breast cancer detection use ~28 kVp x-rays produced by a point source placed 60 cm above the image receptor, centered on the chest wall (Fig. 1.29, left). Without a collimating grid placed above the receptor to reduce the scattered radiation, the typical ratio of scattered-to-primary radiation at the receptor ranges from 0.3 to 1.0, reducing both the signal-to-noise ratio and contrast in diagnostic images. Our goal is the development of a collimating grid with: (1) an air core, (2) lamellar walls oriented to the x-ray source, (3) square-shaped lamellae with ~0.5 mm period, (4) lamellae thickness of 25 μm, and (5) an aspect ratio of wall height to wall thickness of ~100. In a cooperative agreement with Creatv Microtech, Inc., we developed a freestanding copper grid, $45 \times 50 \times 1$ mm^3 in size, with uniform, parallel, smooth, void-free walls, and an aspect ratio exceeding 40 (Fig. 1.29, right) using graphite substrates (Makarova et al., 2002).

1.8.6 Development of a Hard X-ray Nanoprobe at the APS

A new Center for Nanoscale Materials (CNM) is planned for Argonne National Laboratory. The scientific scope of the CNM embraces the fabrication and exploration of novel nanoscale materials that give rise to new properties and phenomena. A next-generation x-ray beamline at the APS will be a cornerstone of the characterization tools available for nanoscience at the CNM. The x-ray nanoprobe (Fig. 1.30) will be a second-generation hard x-ray probe facility with a spatial resolution of 30 nm, covering an

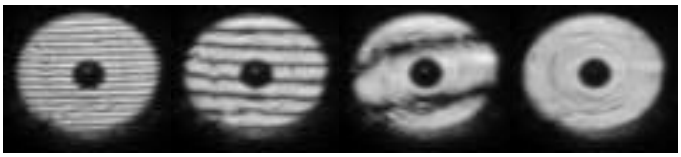

Fig. 1.28. Left: Interference patterns obtained with various transverse displacements of two stacked zone plates. The spatial frequency of the interference fringes becomes zero as the two zone plates are aligned. Right: HXRM and diffractometer in the 2-ID-D station. The x-ray beam enters from the left.

energy range from 3 keV – 30 keV. It will combine diffraction, x-ray fluorescence, and full-field imaging with absorption and phase contrast in a single instrument to study nanomaterials and nanostructures, with particular emphasis on the study of embedded structures. The nanoprobe, in its various operational modes, will allow real space mapping of (1) density and elemental composition through transmission, (2) crystallographic phase, strain, and texture through diffraction, (3) trace elements through fluorescence, (4) chemical states through spectroscopy, (5) magnetic domain structure through linear and circular dichroism, and (6) morphology through tomography. The nanoprobe will be a versatile tool that can be used, for example, to image and track domain evolution in ferroelectric and magnetic nanostructures, to observe strains in microelectronic interconnects, to measure composition and phase distributions in layered nanoparticles for catalysis, or to determine the position and chemical state of hybrid inorganic/organic nanoparticles interacting with biological systems.

1.9 High-Resolution X-ray Scattering

The High-Resolution X-ray Scattering (HRX) Group's activities are focused on developing x-ray optics and applications in nuclear resonant scattering, inelastic x-ray scattering**,** and other applications of high-resolution x-ray scattering techniques to fundamental measurements with resolution power exceeding 10^7 in the hard x-ray regime between 6-30 keV. The development emphasis is on mono-chromators, analyzers, detectors, software, and methodology.

Inelastic nuclear resonant scattering allows direct determination of partial phonon density of states in samples containing a suitable isotope with a low-energy nuclear transition with sub-meV energy resolution. **Coherent nuclear resonant scattering** allows determination of electronic and atomic structure around the probe atom through measurements of hyperfine interaction parameters in the neV energy scale. This is a particularly interesting area for nanoscale magnetism in thin films and multilayers, especially when combined with polarization-selective x-ray scattering techniques at nuclear resonance energy.

Fig. 1.29. Left: Ideal collimating grid with square septa oriented to a point x-ray source at 60 cm. Right: Copper septa are 25 μm thick and over 1,000 μm high (aspect ratio >40).